

1 **Contrasting opacity of bridgmanite and ferropericlase in the lowermost mantle:**

2 **Implications to radiative and electrical conductivity**

3 Sergey S. Lobanov^{1,2,*}, François Soubiran³, Nicholas Holtgrewe², James Badro⁴, Jung-Fu Lin⁵,

4 Alexander F. Goncharov²

5 ¹GFZ German Research Center for Geosciences, Section 3.6, Telegrafenberg, 14473 Potsdam,

6 Germany

7 ²Earth and Planets Laboratory, Carnegie Institution of Washington, Washington, DC 20015,

8 USA

9 ³École Normale Supérieure de Lyon, Université Lyon 1, Laboratoire de Géologie de Lyon,

10 CNRS UMR5276, 69364 Lyon Cedex 07, France

11 ⁴Institut de physique du globe de Paris, Université de Paris, CNRS, 75005 Paris, France

12 ⁵Department of Geological Sciences, Jackson School of Geosciences, The University of Texas at

13 Austin, Austin, Texas 78712, USA

14 *E-mail: slobanov@gfz-potsdam.de

15 **ABSTRACT**

16 Earth's lowermost mantle displays complex geological phenomena that likely result from its
17 heterogeneous physical interaction with the core. Geophysical models of core-mantle interaction
18 rely on the thermal and electrical conductivities of appropriate geomaterials which, however,
19 have never been probed at representative pressure and temperature (*P-T*) conditions. Here we
20 report on the opacity of single crystalline bridgmanite and ferropericlase and link it to their
21 radiative and electrical conductivities. Our results show that light absorption in the visible
22 spectral range is enhanced upon heating in both minerals but the rate of change in opacity with
23 temperature is a factor of six higher in ferropericlase. As a result, bridgmanite in the lowermost

24 mantle is moderately transparent while ferropericlase is highly opaque. Our measurements
25 support previous indirect estimates of low (< 1 W/m/K) and largely temperature-independent
26 radiative conductivity in the lowermost mantle. This implies that the radiative mechanism has
27 not contributed significantly to cooling the Earth's core throughout the geologic time. Opaque
28 ferropericlase is electrically conducting and mediates strong core-mantle electromagnetic
29 coupling, explaining the intradecadal oscillations in the length of day, low secular geomagnetic
30 variations in Central Pacific, and the preferred paths of geomagnetic pole reversals.

31 **Keywords**

32 Thermal conductivity; high pressure; time-resolved spectroscopy; core-mantle boundary;;
33 bridgmanite; ferropericlase;

34

35 1. INTRODUCTION

36 The observed vigor of plate tectonics, plume activity, and geodynamo requires that the present-
37 day heat flow across the core-mantle boundary (Q_{CMB}) is 8-16 TW (Lay et al., 2008; Nimmo,
38 2015). This estimate can be validated independently by employing the Fourier law of heat
39 conduction: $Q_{CMB} = A_{CMB} * k_{total} * \Delta T$ (Eq. 1), where A_{CMB} is the surface area of the CMB, ΔT
40 is the temperature gradient in the thermal boundary layer (TBL), and k_{total} its thermal
41 conductivity. Three microscopic mechanisms of heat transport contribute to k_{total} : lattice,
42 electronic, and radiative thermal conductivities. While all of these contributions have never been
43 measured at CMB P - T conditions, radiative conductivity (k_{rad}) is most uncertain with available
44 estimates spanning 0.35-10 W/m/K (Goncharov et al., 2008; Goncharov et al., 2015; Hofmeister,
45 2014; Keppler et al., 2008; Lobanov et al., 2016; Lobanov et al., 2020). This enormous
46 ambiguity in radiative conductivity, as well as the uncertainty in ΔT and its global variation,
47 precludes tighter constraints on the present-day Q_{CMB} . To better resolve the ability of the mantle
48 to conduct heat via light radiation one needs to measure the optical absorption coefficients of
49 representative lower mantle minerals at CMB P - T conditions.

50 Independent of heat, solid mantle and liquid outer core may exchange angular momenta, which
51 may produce observable variations in Earth's rotation. For example, electromagnetic coupling
52 between the core and mantle may be responsible for the reversible change in the length of day
53 with a period of ~ 6 years (Holme and de Viron, 2013) as detected by geodetic techniques. Strong
54 coupling, however, demands that the direct current (DC) electrical conductivity of the lower
55 mantle minerals is sufficiently high at the CMB (Buffett, 1992). The absence of a significant lag
56 between the rotational and magnetic signals impose a stringent limitation on the thickness of the
57 conducting layer to be smaller than 50 kilometers (Holme and de Viron, 2013). Tomographic
58 images of the lowermost mantle revealed anomalous 5-40 km thick patches directly above the
59 core with strong seismic wave speed reductions of ~ 10 %, called ultra-low velocity zones
60 (ULVZs) (Garnero and McNamara, 2008). Because of their location just above the CMB and

61 small thickness, these patches may be responsible for the efficient core-mantle electromagnetic
62 coupling, yet the electrical properties of ULVZs are unknown. The DC electrical conductivity
63 can be constrained in optical absorption experiments by extrapolating the energy-dependent
64 optical conductivity to zero frequency. Therefore, the radiative and DC electrical conductivities
65 can be in principle determined in a single optical experiment.

66 The optical absorption coefficients of lower mantle minerals have never been measured at CMB
67 P - T conditions ($P \sim 135$ GPa, $T \sim 4000$ K). The brightness of conventional light sources is
68 insufficient to probe hot samples with spectral radiance corresponding to several thousand
69 degrees Kelvin and spectroscopic measurements at the conditions of combined high P and T
70 remain a great challenge. As a consequence, information on the optical properties of mantle
71 minerals at high P is largely limited to $T < \sim 1000$ K. One notable exception is the recent report
72 on the optical extinction coefficients (absorption + scattering) of a polycrystalline assemblage of
73 mostly bridgmanite and ferropericlase (termed pyrolite) at P of up to 135 GPa and T of up to
74 ~ 2800 K that point to an ultra-low radiative conductivity at the CMB of ~ 0.35 W/m/K (Lobanov
75 et al., 2020). The use of a polycrystalline sample with submicron grains in this study allowed
76 minimizing iron diffusion within the sample on the experimental time scale of a few seconds.
77 However, disentangling the absorption and scattering contributions to the measured extinction
78 coefficient of the polycrystalline sample was a principal challenge of that study (Lobanov et al.,
79 2020).

80 Here, we overcome the experimental limitations associated with iron diffusion by reducing the
81 laser-heating duration by a factor of up to $\sim 10^6$, thanks to the use of dynamically-heated diamond
82 anvil cells (DACs) coupled with laser-bright broadband pulsed optical probes and a fast detector.
83 We report the optical absorption coefficients of single crystalline bridgmanite (Bgm),
84 ferropericlase (Fp), and their polycrystalline $\sim 4:1$ aggregate (synthesized from homogeneous
85 pyrolite glass as in described by Lobanov et al. (2020)) to show that temperature is a major
86 factor that governs the opacity near the base of the mantle where Bgm remains moderately

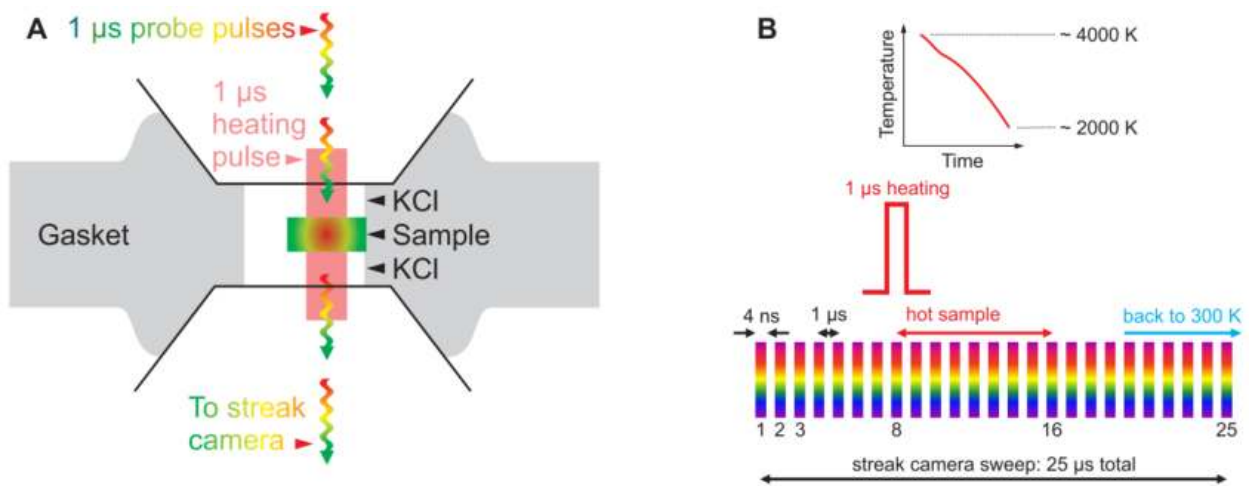
87 transparent in the visible range while Fp is highly opaque. We reinforce our experimental
88 findings with first-principles calculations of Fp optical properties at near CMB conditions, which
89 constrain its absorption coefficient in the near-IR range as well as the electrical conductivity. Our
90 results indicate extremely low radiative thermal contribution to the Q_{CMB} and have profound
91 implications to energy transport and electromagnetic coupling across the core-mantle boundary.

92 2. METHODS

93 2.1.

94 Diamond anvil cell and sample assembly

95 Rhenium gaskets were indented by compression to a pressure of ~ 30 GPa in diamond anvil cells
96 equipped with beveled anvils having 100/300 and 80/300 μm culets. Subsequently, circular holes
97 with a diameter of ~ 50 μm were laser-drilled in the center of the indentation to serve as sample
98 containers. After the drilling, the gaskets were washed in isopropanol for 30 min and mounted
99 between the diamond anvils. Prior to positioning the sample, wafers of dry KCl (5 μm thick)
100 were centered on each of the anvil. Next, double-polished single crystals of ferropericlase
101 ($\text{Mg}_{0.87}\text{Fe}_{0.13}\text{O}$), bridgmanite ($\text{Mg}_{0.94}\text{Fe}^{2+}_{0.04}\text{Fe}^{3+}_{0.02}\text{Al}_{0.01}\text{Si}_{0.99}\text{O}_3$), and pyrolite glass with initial
102 thickness of ~ 8 -16 μm were put into the sample cavity such that a sufficient area of the sample
103 cavity was not covered by the sample to allow for reference transmission measurements through
104 KCl (Fig. 1A). Synthesis procedures for these samples have been reported elsewhere (Lobanov
105 et al., 2020; Lobanov and Speziale, 2019; Mao et al., 2017). Finally, the cells were brought to a
106 desired pressure as gauged either by the position of the diamond Raman edge (Akahama and
107 Kawamura, 2006) or ruby fluorescence (Syassen, 2008). A typical discrepancy between these
108 reading yields the ambiguity in the pressure estimate of $< 5\%$. No correction for thermal
109 pressure was applied since added thermal pressure is smaller than 5 GPa at 3000 K (Goncharov
110 et al., 2007; McWilliams et al., 2016).



111

112 **Figure 1.** (A) Diamond anvil cell assemblage used in this work. Samples were sandwiched between two KCl
 113 and positioned in the cavity such that part of it can be used to measure optical reference (through KCl only). (B)
 114 Timing of our single laser-heating shot experiments. Probe pulses (supercontinuum laser) traverse the sample every
 115 1 μ s. The 1 μ s heating laser (1070 nm, double-sided) arrives at 8 μ s of the 25-30 μ s long streak camera sweep.

116 **2.2.**

117 **Static optical measurements at high pressure and 300 K**

118 Here we used a custom-built all-reflective microscope combined with an IR, VIS, and near-UV
 119 conventional (non-laser) light sources. For the visible and near-UV range we used a fiber-
 120 coupled halogen-D₂ lamp focused to a \sim 50 μ m spot on the sample. The transmitted portion of the
 121 radiation was collimated by a 20 μ m pinhole and sent to the spectrograph (Acton Research
 122 Corporation SpectraPro 500-i) equipped with a 300 grooves/mm grating and a CCD chilled to
 123 235 K. Measurements in the IR range were performed on the same optical bench but with a
 124 Fourier transform spectrometer equipped with a quartz beamsplitter (Varian Resolution Pro 670-
 125 IR). Details of our IR-VIS-UV setup have been reported in our previous publications
 126 (Goncharov et al., 2009; Goncharov et al., 2015; Lobanov et al., 2015; Lobanov et al., 2017b).
 127 Overall, this setup allows for a high-quality absorption spectrum in a wide spectral range (2500-
 128 30000 cm^{-1}) at room temperature. Absorption coefficient was evaluated as $\alpha(\nu) = \ln(10) * \frac{1}{d} * (-\log_{10}(I_{\text{sample}} - I_{\text{bckg}})/(I_{\text{reference}} - I_{\text{bckg}}))$, where d is sample thickness at high pressure
 129 (measured by 3D profilometry on decompressed samples as detailed in the Supplementary
 130 Information), I_{sample} is the intensity of light transmitted through the sample, $I_{\text{reference}}$ is the

132 intensity of light passed through the KCl pressure medium, and I_{bckg} is the background reading.
133 Light losses due to the reflections at the sample-KCl interfaces are small ($< 1\%$) due to the
134 similarity of the KCl and samples' refractive index at $P > 100$ GPa ($n \sim 2$) and were not taken
135 into account.

136 2.3.

137 Static optical measurements at high pressure and $T < \sim 2000$ K

138 Overall, static optical measurements at continuous laser heating allows probing the sample by a
139 large number of probe pulses, which improves the quality of the resulting absorption spectra as
140 compared to spectroscopic measurements in dynamic experiments. The experimental setup
141 combines a quasi-continuous Yt-doped 1070 nm fiber laser, a pulsed Leukos Pegasus ultra-bright
142 supercontinuum (broadband, ~ 4000 - 25000 cm^{-1}) probe operating at 1 MHz, and an intensified
143 gated CCD detector (Andor iStar SR-303i-A). The confocal probe spot size (~ 5 μm) was smaller
144 than the heating laser spot (~ 15 μm). The spectral collection was initiated 500 ms after the start
145 of a 1 s laser heating cycle. The detector gates were modulated for 200 ms at a rate of ~ 41 kHz
146 and synchronized with the probe pulses (4 ns pulse width). Probe brightness was maximized to
147 achieve maximum signal through the reference KCl without saturating the detector. The precise
148 synchronization of the probe pulses and detector gates diminishes thermal background,
149 drastically improves the signal-to-background ratio, and allows optical absorbance
150 measurements in the VIS range (~ 13000 - 22500 cm^{-1}) up to ~ 2000 K. High-temperature
151 absorption coefficients were evaluated as $\alpha(\nu) = \ln(10) * \frac{1}{d} * (-\log_{10}(I_{sample}^T - I_{bckg}^T) / (I_{reference} - I_{bckg}))$, where I_{sample}^T and I_{bckg}^T are the probe and
152 background intensity at high temperature. Temperature was measured from both sides of the
153 sample by imaging the hot spot onto the intensified CCD detector array. In static measurements,
154 the error in temperature is standard to that typically assumed for the laser-heated DAC method (\pm
155 200 K). Further details of this setup can be in Lobanov et al. (2016).
156

157 2.4.

158 **Dynamic optical measurements at high pressure and $T > \sim 2000$ K**

159 To succeed in measuring optical absorption at CMB conditions we performed dynamically-
160 heated experiments with transient optical probing, which is the main novelty of the present work
161 (Fig. 1A). This experimental setup combines the same heating and probe lasers (see above) but
162 spectral measurements were performed by a Sydor ROSS 1000 streak on a Princeton Instruments
163 spectrometer (f/4, 150 grooves/mm). Together these components enable single-pulse laser
164 heating coupled with *in situ* time-resolved absorption measurements at $T > \sim 2000$ K (Jiang et
165 al., 2018). Typical streak camera sweeps were 25-30 μ s long and, accordingly, recorded 25-30
166 pulses of the 1 MHz probe each of which can be used for spectra evaluation (Fig. 1B).

167 Importantly, spectral features and intensity of individual supercontinuum pulses are sufficiently
168 reproducible to allow for single pulse spectroscopy (as is shown in this work). After initiation of
169 the streak camera image collection, a single 1 μ s long pulse of the 1070 nm fiber laser arrives at
170 the 8th μ s to heat the sample (Fig. 1B), allowing for a sufficient number of probe pulses to
171 traverse the sample prior to heating. Sample absorption at high temperature was recorded by the
172 streak camera images (Fig. 2) taken at two distinct grating positions centered at 700 and 590 nm,
173 accessing 15000-20000 and 13000-16400 cm^{-1} spectral ranges, respectively. From streak camera
174 images the absorption coefficient was evaluated as: $\alpha(\nu) = \ln(10) * \frac{1}{d} *$

175 $(- \log_{10}(I_{sample}^{time} - I_{bckg}^{time}) / (I_{reference} - I_{bckg}))$, where I_{sample}^{time} and I_{bckg}^{time} are the probe intensity
176 at a given time and the corresponding (thermal) background. Similarly to the static optical
177 experiments, reflection losses were unimportant.

178 Overlapping absorption spectra were stitched together to produce a spectrum in the 13000-20000
179 cm^{-1} range (Fig. 3). Immediately after the collection of streak camera images the probe laser was
180 blocked and streak camera images were measured again at identical laser heating power. These
181 latter images were used to infer the temperature evolution of the sample for a given laser heating

182 power. In addition, the images of clean thermal background (collected under identical heating
183 power but with the probe laser being blocked) were used to obtain I_{bckg}^{time} . Temperature
184 measurements at the 700 and 590 nm grating position generally yielded consistent results.
185 However, temperature measurements with the grating centered at 590 nm often yielded
186 temperatures lower than that at obtained at the 700 nm grating position (up to 1200 K lower). To
187 assign temperatures to stitched spectra we relied on radiometry measurements with the grating
188 centered at 700 nm, as more light was available for Planck fitting, which improves the reliability
189 in temperature determination. We could only observe sufficiently intense thermal background ($>$
190 10 counts in a single streak camera sweep) at $T > \sim 3000$ K. To characterize sample absorbencies
191 at lower temperatures, up to 100 consecutive streak camera sweeps were accumulated at low
192 laser heating power to improve the statistics, assuming that the coupling of the sample to the
193 heating laser did not change substantially over the 100 heating cycles. In all cases, the sample
194 absorbance was checked afterwards to ensure its reversibility over the heating cycles.

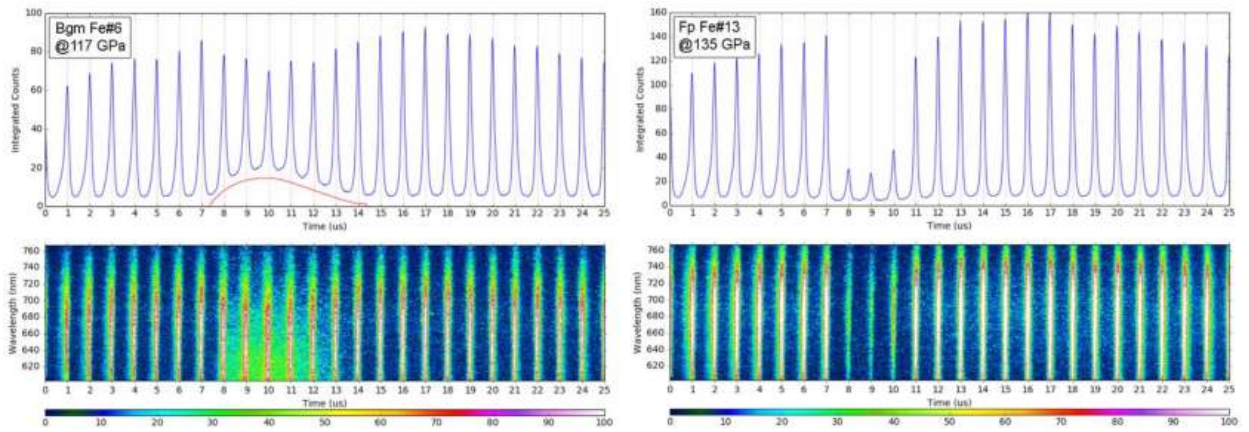
195 We estimate the overall temperature uncertainty based on the reproducibility of the absorption
196 coefficients at high temperatures. At $T > 2000$ K, the reproducibility of the absorption
197 coefficients was typically within 0-20 %, which translates to the overall ambiguity in the
198 temperature measurements of $< \pm 500$ K. This estimate is independently confirmed by optical
199 observations of dark spots (presumably Fe-rich and formed upon melting) and increased room-
200 temperature absorbencies in samples quenched from temperatures exceeding their expected
201 solidus.

202 3. RESULTS AND DISCUSSION

203 First, we collected high-pressure wide spectral range absorption coefficients of double-polished
204 single crystalline Bgm6 (Bgm with 6 mol.% Fe) and Fp13 (Fp with 13 mol.% Fe) (Fig. S1) using
205 a conventional optical absorption setup that allows high-quality measurements at room
206 temperature (Goncharov et al., 2009). These absorption spectra reveal the distinct light

207 absorption mechanisms that may contribute to the opacity of Bgm and Fp in the lowermost
208 mantle. Intervalence Fe^{2+} - Fe^{3+} charge transfer (CT) gives rise to the broad absorption band at
209 $\sim 17000 \text{ cm}^{-1}$ in the spectrum of Bgm6 ($\text{Mg}_{0.94}\text{Fe}^{2+}_{0.04}\text{Fe}^{3+}_{0.02}\text{Al}_{0.01}\text{Si}_{0.99}\text{O}_3$), which is close in
210 composition to that expected for Bgm in the lower mantle (Mao et al., 2017). Crystal field ($d-d$)
211 bands were not observed in the thin ($\sim 6 \mu\text{m}$ at 117 GPa) and relatively iron-poor sample studied
212 here, as was also the case in the previous high-pressure studies of lower mantle Bgm (Goncharov
213 et al., 2015; Keppler et al., 2008). The spectrum of Fp13 showed three multiplicity-allowed low
214 spin Fe^{2+} bands. Both Bgm6 and Fp13 have a distinct UV absorption edge, typically assigned to
215 the Fe-O CT (Burns, 1993).

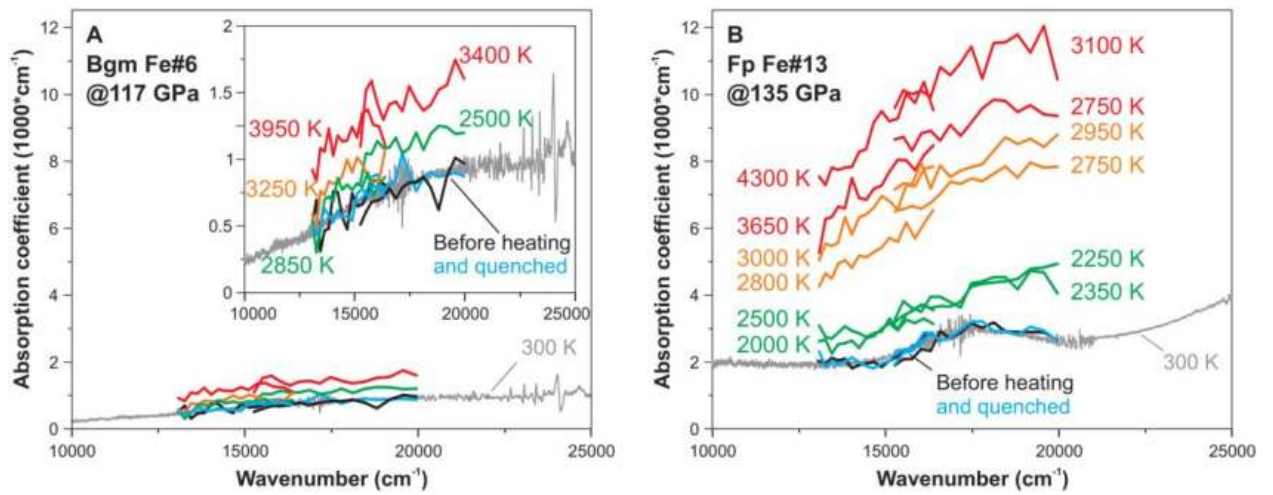
216 We continued with dynamic experiments in which the samples were heated by a single $1 \mu\text{s}$ long
217 near-infrared (1070 nm) laser pulse and probed by an ultra-bright broadband pulsed laser.
218 Thermal radiation emitted off the dynamically-heated samples vanishes in streak camera images
219 within $\sim 10 \mu\text{s}$ following the arrival of the heating pulse (Fig. 2). Finite-element modeling of
220 time-dependent thermal fluxes in a pulsed laser-heated DAC also indicates that $\sim 10 \mu\text{s}$ is
221 sufficient to restore sample's temperature back to 300 K, thanks to the high thermal conductivity
222 of diamond (Montoya and Goncharov, 2012). Accordingly, the probe pulse train arriving with an
223 interval of $1 \mu\text{s}$ traverses distinct thermal states and records the spectroscopic information in time
224 domain. The timing of our dynamic experiments also allows extracting room-temperature
225 absorption spectra prior to the arrival of the heating laser and after quenching. The obtained
226 room-temperature spectra were in good agreement with our wide-range spectra.



227

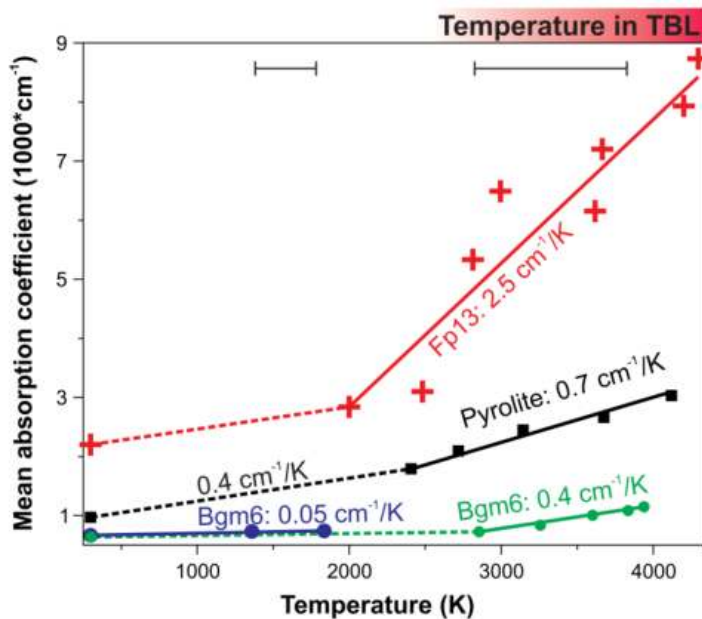
228 **Figure 2.** Representative streak camera images (bottom panels) and corresponding integrated intensity (top panels)
 229 of Bgm6 at 117 GPa (left) and Fp13 at 135 GPa (right). The 1 μ s laser heating pulse arrived at $\sim 8^{\text{th}}$ microsecond
 230 heating the samples to a maximum temperature of ~ 4000 K (Bgm) and ~ 3000 K (Fp), in these particular shots. Note
 231 the presence of apparent thermal background in the case of bridgmanite (top panel, red curve).

232 Upon heating of Bgm6 to ~ 2500 K its absorption coefficient (α) is enhanced by approximately a
 233 factor of two (Fig. 3), translating into a relatively small rate of increase in opacity averaged over
 234 the visible range: $\Delta\alpha/\Delta T$ of ~ 0.05 cm^{-1}/K (Fig. 4). At $T > \sim 3000$ K, Bgm6 visible range opacity
 235 increases much more rapidly with $\Delta\alpha/\Delta T = 0.4$ cm^{-1}/K , suggesting a crossover to a more efficient
 236 light absorption mechanism in Bgm across the temperature range of the TBL. Similarly, the
 237 opacity of Fp13 is enhanced at $T > 2000$ K but with a rate that is approximately six times faster
 238 than in Bgm6 ($\Delta\alpha/\Delta T = 2.5$ cm^{-1}/K). Specific absorption bands are no longer resolved in the
 239 high-temperature spectra of Bgm6 and Fp13 and the visible range opacity is evidently governed
 240 by a reversible temperature-induced red-shift of the Fe-O CT (UV absorption edge). Indeed, the
 241 initial room-temperature absorption coefficients of Bgm6 and Fp13 are restored after the samples
 242 cool down to 300 K. The reversibility in opacity over the heating cycles indicates that our pulsed
 243 laser heating time domain experiments probe intrinsic temperature-induced changes in the
 244 electronic structure as opposed to extrinsic iron redistribution due to temperature gradients in
 245 continuously laser-heated sample.



246

247 **Figure 3.** Absorption coefficients of bridgmanite at 117 GPa (A) and ferropericlase at 135 GPa (B). Black – prior to
 248 the heating pulse arrival (1-7 μ s); red, orange, or green – upon cooling at high temperature (9-16 μ s); and blue –
 249 after cooling (20-25 μ s). The spectra are labeled by apparent temperatures measured immediately after the
 250 absorbance measurements at identical laser heating power. The discrepancy in temperature among the overlapping
 251 spectra is probably due to more less reliable temperature measurements at higher frequencies. The assignment of
 252 temperature to the measured spectra was based on the lower frequency spectral range (13100-16400 cm^{-1}), which
 253 also yields more conservatives estimate of opacity. Inset in (A) is a close-up view of Bgm6 data. Temperature
 254 uncertainty is ± 500 K. Grey spectra are absorption coefficients measured prior to heating with a conventional
 255 absorption spectroscopy setup (Goncharov et al., 2009). Corresponding wide-range spectra (SWIR to UV) at 300 K
 256 are shown in Fig. S1.



257

258 **Figure 4.** Temperature dependence of the mean absorption coefficients (13100-16400 cm^{-1}) observed in dynamic
259 laser-heating experiments on bridgmanite at 117 GPa (Bgm6, green), ferropericlase at 135 GPa (Fp13, red), and
260 pyrolite at 130 GPa (black). Dashed lines show an extrapolation from the 2500-3000 K data to 300 K. The violet
261 solid line shows the mean absorption coefficient of Bgm6 obtained in static laser-heating experiments (Fig. S2),
262 which is in agreement with that reported previously ($\sim 0.08 \text{ cm}^{-1}/\text{K}$ at $\sim 1600\text{-}2500 \text{ K}$) for the same crystal at 87 GPa
263 (Lobanov et al., 2020). Error bars indicate the temperature uncertainty of $\sim \pm 500 \text{ K}$ and $\sim \pm 200 \text{ K}$ in dynamic ($T >$
264 $\sim 2000 \text{ K}$) and static ($T < \sim 2000 \text{ K}$) experiments, respectively. The red bar above the figure depicts the temperature
265 increase expected in the thermal boundary layer (TBL).

266 To gain quantitative information on the opacity of Bgm and Fp at $T < 2000 \text{ K}$ the same DAC
267 loadings were used for static optical absorption experiments in which the samples were
268 continuously laser-heated for 1s and probed by the broadband pulsed laser synchronized with a
269 gated detector. Heating of Bgm6 to $\sim 2000 \text{ K}$ results in a slight decrease of its $\text{Fe}^{2+}\text{-Fe}^{3+}$ CT band
270 intensity while the contribution of the UV absorption edge is enhanced (Fig. S2). This static
271 experiment reveals the competition of individual light absorption mechanisms in Bgm6 at $T <$
272 2000 K , which is the cause of the relatively small net increase of its opacity in this temperature
273 range ($\Delta\alpha/\Delta T = 0.05 \text{ cm}^{-1}/\text{K}$), in excellent agreement with the rate inferred from the dynamic
274 experiments described above (Fig. 4). Unfortunately, in static experiments on Fp13 we could not
275 achieve satisfactory spectra reversibility at $T > 1000 \text{ K}$, which we tentatively assign to Soret-like
276 iron diffusion due to the unavoidable temperature gradients in a laser-heated DAC. Note that the
277 iron diffusivity in Fp is several orders of magnitude higher than in Bgm (Ammann et al., 2011).
278 The use of a single and short laser-heating pulse in dynamic experiments described in this work
279 allowed us to suppress this unwanted irreversible effects in single crystals and build up on our
280 previous study of pyrolite optical properties at static P - T conditions (Lobanov et al., 2020).

281 The crossover in the slope of $\Delta\alpha/\Delta T$ in Bgm and Fp at $T > 2000 \text{ K}$ indicates a transition to the
282 opacity regime dominated by the Fe-O CT, which is centered in the UV and is much more
283 intense than d - d or $\text{Fe}^{2+}\text{-Fe}^{3+}$ transitions because electronic states of different parity (d and p) are
284 involved in the excitation. Thus, the visible range opacity of Bgm and Fp in the lowermost

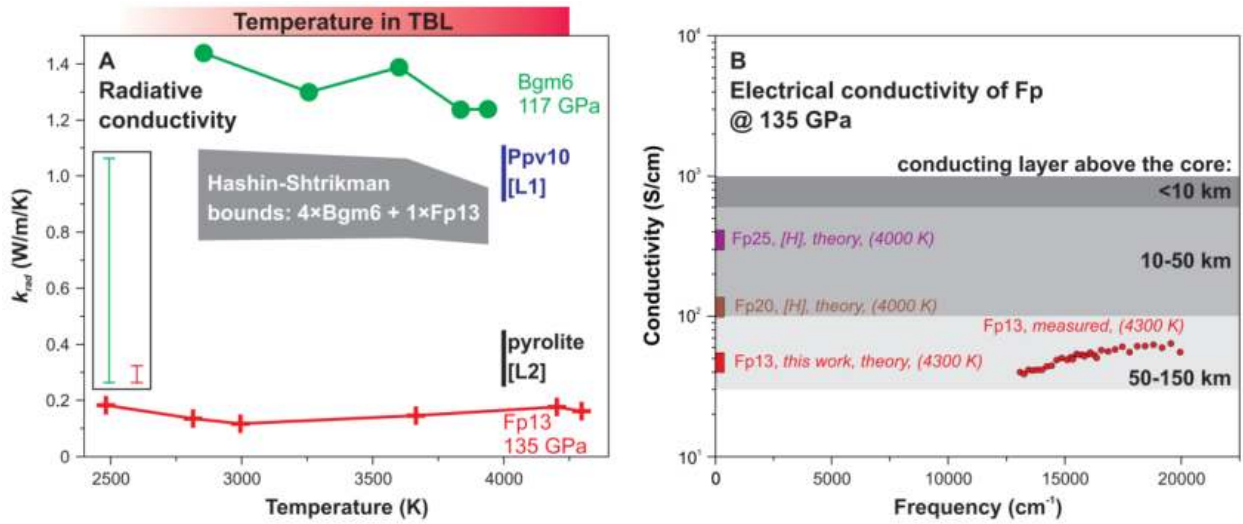
285 mantle is governed by the Fe-O p - d orbital overlap. Iron in the studied Bgm6 sample is
286 predominantly eightfold-coordinated (distorted pseudododecahedral site) (Mao et al., 2017)
287 while Fp hosts iron exclusively at the octahedral site. The p - d orbital overlap at the sixfold site in
288 Fp is definitely larger than that at the twelvefold site in Bgm by virtue of a shorter Fe-O bond in
289 Fp. As a result, the contribution of the Fe-O CT to the visible range absorbance is stronger in Fp
290 and the corresponding $\Delta\alpha/\Delta T$ (*i.e.* temperature-induced red-shift) is a factor of six higher than in
291 Bgm. Temperature-induced red-shifts of the Fe-O CT band have been identified in many
292 ferromagnesian minerals at relatively low pressure and $T < 1700$ K (*e.g.* Refs.(Burns, 1993;
293 Lobanov et al., 2016; Shankland et al., 1979)), but the effect this mechanism bears on the lower
294 mantle opacity and by extension its transport properties has never been quantified.

295 To understand the combined effect of Bgm and Fp on the opacity of the lower mantle in a
296 realistic representative composition, we performed dynamic-heating optical experiments on
297 pyrolite at 130 GPa and up to ~ 4000 K (Fig. S3). We find that at $T > 2500$ K the absorption
298 coefficient of pyrolite increases with $0.7 \text{ cm}^{-1}/\text{K}$, in excellent agreement with the expectation
299 ($\Delta\alpha/\Delta T = 0.8 \text{ cm}^{-1}/\text{K}$) for a hypothetical 4:1 mechanical mixture of Bgm with Fp (*i.e.* constructed
300 by weighing the opacity slopes of Bgm and Fp (Fig. 4) with their approximate volume fractions
301 in the pyrolite model). Extrapolating dynamic-heating data to $T < 2500$ K points to a factor of
302 two smaller $\Delta\alpha/\Delta T$ of $\sim 0.4 \text{ cm}^{-1}/\text{K}$, also in agreement with that reported recently for the same
303 pyrolite sample but in static-heating optical experiments at 135 GPa and $T < 2700$ K (Lobanov et
304 al., 2020). The derived absolute value of the mean absorption coefficient at 300 K for such a
305 pyrolite composition is sensitive to the scattering correction applied to compensate for light
306 scattering on grain boundaries. Here, we estimated the contribution of scattering to the measured
307 light extinction coefficient (absorption coefficient + scattering coefficient) in pyrolite based on
308 the 300 K absorption coefficients of Bgm6 and Fp13 (Fig. S1), which is appropriate because
309 scattering is negligible in single crystals. First, we constructed a hypothetical room-temperature
310 absorption coefficient of the mechanical mixture of Bgm6 with Fp13 in the 4:1 proportion

311 (pyrolite model) to infer that at 300 K the mean absorption coefficient of pyrolite in the visible
312 range is $\sim 1000 \text{ cm}^{-1}$. The scattering coefficient at 300 K is then obtained by subtracting the value
313 of 1000 cm^{-1} from the pyrolite extinction coefficient measured at 300 K. Assuming light
314 scattering does not change significantly with T , we obtain the absorption coefficients of pyrolite
315 at high T from the measured extinction coefficients by subtracting the scattering contribution
316 (Fig. S3). In any case, the extracted values of $\Delta\alpha/\Delta T$ for pyrolite (Fig. 4) are robust as they do
317 not depend on the scattering correction. This assumption of a temperature-independent scattering
318 coefficient is rather accurate as values of $\Delta\alpha/\Delta T$ expected for the hypothetical 4:1 mechanical
319 mixture of Bgm and Fp (pyrolite model) based on the single crystal measurements and that
320 measured directly in pyrolite are in excellent agreement. Significant grain growth over the $1 \mu\text{s}$
321 heating cycle, which would affect the scattering at high T , can also be ruled out since the
322 temperature-enhanced absorbance of pyrolite is fully reversible (Fig. S3).

323 In addition to the visible range opacity, we need to constrain the opacity in the near-IR spectra
324 range, where most of the radiative flux is expected at all plausible mantle temperatures. Towards
325 this end, we computed the electronic structure of $(\text{Mg}_{0.875}\text{Fe}_{0.125})\text{O}$ (Supplementary Information)
326 at P - T conditions mimicking that in our optical experiments (135 GPa, 4300 K). The computed
327 electronic density of states (DOS) shows a non-zero density of d -electrons at the Fermi level due
328 to the overlapping iron d -orbitals (Fig. S4). Local projection of the states identifies the peak
329 centered at -1 eV as the t_{2g} states and the peak centered at $+1 \text{ eV}$ as the e_g states of iron, both
330 mixed with oxygen p states. Electronic excitations between the occupied (centered at -1 and $+0.5$
331 eV) and unoccupied (centered at $+1 \text{ eV}$) states give rise to the distinct absorption bands observed
332 at ~ 0.5 and $\sim 2 \text{ eV}$ (Fig. S5). Oxygen p -electrons also have non-zero DOS near the -1 and $+1 \text{ eV}$
333 levels and likely contribute to the observed absorption because of its higher probability for odd-
334 parity states. We conclude, therefore, that both crystal field (d - d) and Fe-O CT (p - d) transitions
335 are important mechanisms of Fp opacity at CMB conditions.

336 We model radiative thermal conductivity (k_{rad}) in the TBL above the CMB using the
337 experimentally-measured absorption coefficients of Fp and Bgm at 117-135 GPa and 2500-4300
338 K. The measured absorption coefficients of Fp were extrapolated to 3000 cm^{-1} and 25000 cm^{-1}
339 using the Smith-Drude model that allows for a smooth decrease in the absorption coefficient
340 with frequency (Fig. S6A). Using this lower bound constraint on the Fp13 absorption coefficient
341 we can now obtain its radiative thermal conductivity (Supplementary Information): $\sim 0.2\text{ W/m/K}$
342 at 135 GP and 2500-4300 K (Fig. 5A). By extrapolating the absorption coefficients of Bgm6 in a
343 similar fashion (Fig. S6B) we obtain a radiative conductivity in the range of $\sim 1.2\text{-}1.4\text{ W/m/K}$ at
344 $T \sim 3000\text{-}4000\text{ K}$ (Fig. 5A). The radiative conductivity of Bgm may be sensitive to the not-yet-
345 constrained Fe^{3+} content of this phase in the lower mantle. Our anticipation is that ferric iron at
346 the pseudododecahedral site A of Bgm would only have a minor effect on the opacity of Bgm at
347 $T > 2000\text{ K}$ because, as discussed above, the opacity is governed by the p - d overlap of
348 octahedrally-coordinated iron. By the same logic, the substitution of Si for Fe^{3+} at the octahedral
349 site B (Hummer and Fei, 2012) would increase the opacity of Bgm at high temperature. In any
350 case, the obtained k_{rad} values of Bgm and Fp are upper bounds because both these phases are
351 expected to show absorption bands in the IR, which we did not take into account in evaluating
352 radiative conductivity. This may be the reason for the apparent disagreement with the pyrolite
353 k_{rad} model which in turn relies heavily on the scattering correction (Lobanov et al., 2020). The
354 geophysical significance of our estimates of radiative conductivity is secondary because it is
355 approximately four times smaller than the most conservative estimates of lattice thermal
356 conductivity of $\sim 4\text{-}5\text{ W/m/K}$ (Tang et al., 2014). Most previous estimates of lattice thermal
357 conductivity at the base of the mantle, however, group at $\sim 6\text{-}14\text{ W/m/K}$ (Geballe et al., 2020;
358 Haigis et al., 2012; Hsieh et al., 2017, 2018; Manthilake et al., 2011; Ohta et al., 2017; Ohta et
359 al., 2012; Okuda et al., 2020; Okuda et al., 2017; Stackhouse et al., 2015).



360

361 **Figure 5. (A)** Radiative conductivity of ferropericlasite ($\text{Mg}_{0.87}\text{Fe}_{0.13}\text{O}$) and bridgmanite
 362 ($\text{Mg}_{0.94}\text{Fe}^{2+}_{0.04}\text{Fe}^{3+}_{0.02}\text{Al}_{0.01}\text{Si}_{0.99}\text{O}_3$) at the P - T conditions of the lowermost mantle. The corresponding Hashin-
 363 Shtrikman bounds (Hashin and Shtrikman, 1962) for a mixture of 80 vol.% Bgm and 20 vol.% Fp are shown in grey.
 364 The vertical black and dark blue bars are previous estimates of radiative conductivity for pyrolite (Lobanov et al.,
 365 2020) and post-perovskite (Lobanov et al., 2017a), respectively. The green and red vertical bars in the inset are error
 366 bars estimated as 30 % of the k_{rad} value (Supplementary Information). The horizontal red bar above the figure
 367 depicts the temperature increase expected in the thermal boundary layer (TBL). **(B)** Optical conductivity of
 368 ($\text{Mg}_{0.87}\text{Fe}_{0.13}\text{O}$) measured at 135 GPa and 4300 K (red circles) and the corresponding DC electrical conductivity
 369 (red rectangle). Values for DC electrical conductivity of Fp with higher iron content from Holmstrom et al. (2018).
 370 The grey shaded areas depict the ranges of Fp DC conductivity that would provide a conductance of 10^8 S in the
 371 lowermost 10, 10-50, and 50-150 km when arithmetically mixed with insulating Bgm (0.03 S/cm) (Sinmyo et al.,
 372 2014) in the 1:4 proportion (pyrolite model). The conductance of 10^8 S is required for the core-mantle
 373 electromagnetic coupling sufficient to produce the observed 6 year component in the length of day fluctuations
 374 (Buffett, 1992; Holme and de Viron, 2013).

375 The radiative conductivity of Bgm and Fp at high P - T conditions is essentially temperature-
 376 invariant, unlike that of semi-transparent materials where $k_{rad} \sim \frac{T^3}{\alpha(P,T)}$ (Clark, 1957). Evidently,
 377 the transfer of radiative energy in the lowermost mantle is diminished by the temperature-
 378 induced opacity of Fp and Bgm revealed here. Assuming appropriate volume fractions of Bgm
 379 and Fp in the pyrolitic model (0.8 and 0.2) we obtained the Hashin-Shtrikman bounds (Hashin
 380 and Shtrikman, 1962) on the effective radiative conductivity in the lowermost mantle (Fig. 5A).

381 The present results indicate that the radiative conductivity remains largely constant across the
382 TBL and is smaller than ~ 1 W/m/K. The absorption coefficient of post-perovskite is about two
383 times higher than that of Bgm at the total iron content of ~ 10 mol.% but shows a qualitatively
384 similar temperature-dependence of its individual absorption bands (Lobanov et al., 2017a) to that
385 observed in Bgm in this work due to their crystal chemical similarity. Therefore, the inclusion of
386 post-perovskite into the model would result in lower radiative conductivity values.

387 Our DFT computations also indicate that the electronic contribution to the total thermal
388 conductivity is non-negligible and is ~ 1 W/m/K (Fig. S7), which is consistent with the estimate
389 of Holmstrom et al. (2018) for Fp with 19 mol.% Fe. However, the relatively small volume
390 fraction of Fp (20 vol.%) in the lower mantle suggests that the electronic contribution of Fp to
391 the total thermal conductivity of the lowermost mantle is insignificant (~ 0.2 W/m/K).

392 Accordingly, our estimate of the total thermal conductivity of a pyrolitic mantle ($k_{total} = 4-11$
393 W/m/K) only accounts for the radiative ($k_{rad} = 1$ W/m/K, this work) and lattice contributions (3-
394 10 W/m/K at CMB, previous studies (Geballe et al., 2020; Hsieh et al., 2018; Ohta et al., 2017;
395 Okuda et al., 2017; Stackhouse et al., 2015; Tang et al., 2014)). Using our estimate of total
396 thermal conductivity in Eq.1 we obtain $Q_{CMB} = 1.5-27$ TW for the temperature gradients in the
397 TBL of 0.0025-0.016 K/m (Lay et al., 2008; van der Hilst et al., 2007). That is, the approach
398 based on the Fourier law of heat conduction yields a factor of twenty uncertain Q_{CMB} . While
399 being broadly consistent with the estimates based on the core and mantle dynamics of $Q_{CMB} = 8-$
400 16 TW (Lay et al., 2008; Nimmo, 2015), this result highlights the need for more accurate
401 constraints on thermal conductivity and, especially, temperature gradients in the TBL at the base
402 of the mantle. We note, however, that the apparent invariance of k_{rad} to T found here implies that
403 heat transport by light radiation has remained relatively inefficient throughout geologic time and
404 could not have promoted a higher Q_{CMB} in the hotter ancient Earth.

405 In addition to the heat transport across the CMB, our results offer a cross-check on the geodesy-
406 based inference of high electrical conductance (10^8 S) layer 10-150 km above the core. Here we

407 showed that Bgm is insulating under near-CMB conditions as it remains relatively transparent in
408 the visible range even at $T \sim 4000$ K; thus, the potentially high DC conductivity of the lowermost
409 mantle cannot be due to Bgm. This is also supported by previous studies that inferred a relatively
410 low Bgm (and post-perovskite) electrical conductivity (~ 0.01 - 0.03 S/cm) at high P - T conditions
411 (Ohta et al., 2008; Sinmyo et al., 2014). In contrast to Bgm, the measured absorption coefficients
412 of Fp imply that its DC conductivity is much higher than that of Bgm at near CMB conditions.
413 The computed electrical conductivities of $(\text{Mg}_{0.875}\text{Fe}_{0.125})\text{O}$ at 135 GPa and 4300 K span ~ 45 -
414 165 S/cm (Fig. S8), depending mainly on the band gap correction used in the computation. This
415 result is not only consistent with the recent theoretical estimates (Holmstrom et al., 2018), but it
416 falls within the range of DC conductivities required to produce the conductance of 10^8 S in a 50-
417 150 km thick mixture of insulating Bgm (80 vol.%) with conducting Fp (20 vol.%) (Fig. 5B).
418 The necessary electrical conductance may be achieved even in a thin (*e.g.* < 50 km) layer just
419 above the core if the electrical conductivity of Fp is greater than 100 S/cm. The results of this
420 work together with previous first-principles computations (Holmstrom et al., 2018) are consistent
421 with such high electrical conductivity in iron-enriched Fp (> 20 mol.% Fe), which could be a
422 plausible explanation for the six year oscillation in the length of day (Buffett, 1992; Holme and
423 de Viron, 2013). Seismic tomography images have revealed patches of ULVZs that could be
424 explained by the occurrence of iron-enriched Fp (Wicks et al., 2017). If such, these regions
425 implement strongest core-mantle electromagnetic coupling and may manifest themselves in
426 geomagnetic features observable at the Earth's surface. A large ULVZ located beneath the
427 Central Pacific may electromagnetically screen the varying field of the core (Buffett, 2015;
428 Runcorn, 1992), which would explain the anomalously low geomagnetic secular variations
429 observed in this region at least over the past 10-100 Ka (Constable et al., 2016; Panovska et al.,
430 2018). Likewise, electric currents in a ULVZ triggered by rapid changes in the orientation of the
431 magnetic dipole during geomagnetic reversals may generate a torque on the core and guide the
432 reversing dipole along the meridians that border the ULVZ (Buffett, 2015; Runcorn, 1992).

433 Therefore, the preference of reversal paths that border the Pacific Ocean may be due to the
434 ULVZ detected beneath the Pacific.

435 Overall, our results underscore the link between radiative and electrical conductivity. Moderately
436 opaque and electrically insulating Bgm has small but non-negligible radiative thermal
437 conductivity the magnitude of which determines the radiative heat flux in the lowermost mantle.
438 Highly opaque Fp has negligible radiative thermal conductivity but its semi-metallic electrical
439 conductivity is sufficient to implement efficient core-mantle electromagnetic coupling.
440 Therefore, possible variations in the mineralogical abundances of these minerals along the CMB
441 (*e.g.* in the basaltic and pyrolitic compositions) provide the means for heterogeneous CMB
442 thermal and electromagnetic interaction. Strongest core-mantle electromagnetic interaction is
443 expected in regions where Fp is present at the CMB, which may be detected in the secular signal
444 of Earth's magnetic field.

445 **ACKNOWLEDGEMENTS**

446 SSL acknowledges the support of the Helmholtz Young Investigators Group CLEAR (VH-NG-
447 1325). The authors thank T. Okuchi and N. Purevjav in synthesis of Fp and Bgm samples. FS
448 was supported by a Marie Skłodowska-Curie action under the project ABISSE (grant agreement
449 no. 750901). The work at Carnegie was supported by the NSF (grant numbers DMR-1039807,
450 EAR-1520648, EAR/IF-1128867, and EAR-1763287), the Army Research Office (grant 56122-
451 CH-H), the Deep Carbon Observatory, and the Carnegie Institution of Washington. Numerical
452 simulations were performed on the GENCI supercomputer Occigen through the stl2816 series of
453 eDARI computing grants. JFL acknowledges support by the NSF Geophysics Program (EAR-
454 1446946 and EAR-1916941). JB acknowledges support by IPGP multidisciplinary program
455 PARI, by Région Île de France SESAME Grant no. 12015908, and by Université de Paris
456 UnivEarthS Labex program (ANR-10-LABX-0023 and ANR-11-IDEX-0005-02).

457

- 459 Akahama, Y., Kawamura, H., 2006. Pressure calibration of diamond anvil Raman gauge to 310 GPa. *J.*
460 *Appl. Phys.* 100, 043516.
- 461 Ammann, M.W., Brodholt, J.P., Dobson, D.P., 2011. Ferrous iron diffusion in ferro-periclase across the
462 spin transition. *Earth Planet. Sci. Lett.* 302, 393-402.
- 463 Buffett, B.A., 1992. Constraints on Magnetic Energy and Mantle Conductivity from the Forced Nutations
464 of the Earth. *J. Geophys. Res.: Solid Earth* 97, 19581-19597.
- 465 Buffett, B.A., 2015. 8.08 - Core–Mantle Interactions A2 - Schubert, Gerald, in: Schubert, G. (Ed.), *Treatise*
466 *on Geophysics (Second Edition)*. Elsevier, Oxford, pp. 213-224.
- 467 Burns, R.G., 1993. *Mineralogical applications of crystal field theory*, 2nd ed. Cambridge University Press,
468 U.K.
- 469 Clark, S.P., 1957. Radiative transfer in the Earth's mantle. *Eos (formerly Trans. Am. Geophys. Union)* 38,
470 931-938.
- 471 Constable, C., Korte, M., Panovska, S., 2016. Persistent high paleosecular variation activity in southern
472 hemisphere for at least 10 000 years. *Earth Planet. Sci. Lett.* 453, 78-86.
- 473 Garnero, E.J., McNamara, A.K., 2008. Structure and dynamics of Earth's lower mantle. *Science* 320, 626-
474 628.
- 475 Geballe, Z.M., Sime, N., Badro, J., van Keken, P.E., Goncharov, A.F., 2020. Thermal conductivity near the
476 bottom of the Earth's lower mantle: Measurements of pyrolite up to 120 GPa and 2500 K. *Earth Planet.*
477 *Sci. Lett.* 536, 116161.
- 478 Goncharov, A.F., Beck, P., Struzhkin, V.V., Haugen, B.D., Jacobsen, S.D., 2009. Thermal conductivity of
479 lower-mantle minerals. *Phys. Earth Planet. Inter.* 174, 24-32.
- 480 Goncharov, A.F., Crowhurst, J.C., Dewhurst, J.K., Sharma, S., Sanloup, C., Gregoryanz, E., Guignot, N.,
481 Mezouar, M., 2007. Thermal equation of state of cubic boron nitride: Implications for a high-
482 temperature pressure scale. *Phys. Rev. B* 75, 224114.
- 483 Goncharov, A.F., Haugen, B.D., Struzhkin, V.V., Beck, P., Jacobsen, S.D., 2008. Radiative conductivity in
484 the Earth's lower mantle. *Nature* 456, 231-234.
- 485 Goncharov, A.F., Lobanov, S.S., Tan, X., Hohensee, G.T., Cahill, D.G., Lin, J.F., Thomas, S.M., Okuchi, T.,
486 Tomioka, N., 2015. Experimental study of thermal conductivity at high pressures: Implications for the
487 deep Earth's interior. *Phys. Earth Planet. Inter.* 247, 11-16.
- 488 Haigis, V., Salanne, M., Jahn, S., 2012. Thermal conductivity of MgO, MgSiO₃ perovskite and post-
489 perovskite in the Earth's deep mantle. *Earth Planet. Sci. Lett.* 355, 102-108.
- 490 Hashin, Z., Shtrikman, S., 1962. A variational approach to theory of effective magnetic permeability of
491 multiphase materials. *J. Appl. Phys.* 33, 3125-3131.
- 492 Hofmeister, A.M., 2014. Thermodynamic and optical thickness corrections to diffusive radiative transfer
493 formulations with application to planetary interiors. *Geophys. Res. Lett.* 41, 3074-3080.
- 494 Holme, R., de Viron, O., 2013. Characterization and implications of intradecadal variations in length of
495 day. *Nature* 499, 202-205.
- 496 Holmstrom, E., Stixrude, L., Scipioni, R., Foster, A.S., 2018. Electronic conductivity of solid and liquid (Mg,
497 Fe)O computed from first principles. *Earth Planet. Sci. Lett.* 490, 11-19.
- 498 Hsieh, W.P., Deschamps, F., Okuchi, T., Lin, J.F., 2017. Reduced lattice thermal conductivity of Fe-bearing
499 bridgmanite in Earth's deep mantle. *J. Geophys. Res.: Solid Earth* 122, 4900-4917.
- 500 Hsieh, W.P., Deschamps, F., Okuchi, T., Lin, J.F., 2018. Effects of iron on the lattice thermal conductivity
501 of Earth's deep mantle and implications for mantle dynamics. *Proc. Natl. Acad. Sci. U.S.A.* 115, 4099-
502 4104.
- 503 Hummer, D.R., Fei, Y.W., 2012. Synthesis and crystal chemistry of Fe³⁺-bearing (Mg,Fe³⁺)(Si,Fe³⁺)O₃
504 perovskite. *Am. Mineral.* 97, 1915-1921.
- 505 Jiang, S.Q., Holtgrewe, N., Lobanov, S.S., Su, F.H., Mahmood, M.F., McWilliams, R.S., Goncharov, A.F.,
506 2018. Metallization and molecular dissociation of dense fluid nitrogen. *Nat. Comm.* 9, 2624.
- 507 Keppler, H., Dubrovinsky, L.S., Narygina, O., Kantor, I., 2008. Optical absorption and radiative thermal
508 conductivity of silicate perovskite to 125 Gigapascals. *Science* 322, 1529-1532.
- 509 Lay, T., Hernlund, J., Buffett, B.A., 2008. Core-mantle boundary heat flow. *Nat. Geosci.* 1, 25-32.

510 Lobanov, S.S., Goncharov, A.F., Litasov, K.D., 2015. Optical properties of siderite (FeCO₃) across the spin
511 transition: Crossover to iron-rich carbonates in the lower mantle. *Am. Mineral.* 100, 1059-1064.

512 Lobanov, S.S., Holtgrewe, N., Goncharov, A.F., 2016. Reduced radiative conductivity of low spin FeO₆-
513 octahedra in FeCO₃ at high pressure and temperature. *Earth Planet. Sci. Lett.* 449, 20-25.

514 Lobanov, S.S., Holtgrewe, N., Ito, G., Badro, J., Piet, H., Nabiei, F., Lin, J.-F., Bayarjargal, L., Wirth, R.,
515 Schreiber, A., Goncharov, A.F., 2020. Blocked radiative heat transport in the hot pyrolytic lower mantle.
516 *Earth Planet. Sci. Lett.* 537, 116176.

517 Lobanov, S.S., Holtgrewe, N., Lin, J.F., Goncharov, A.F., 2017a. Radiative conductivity and abundance of
518 post-perovskite in the lowermost mantle. *Earth Planet. Sci. Lett.* 479, 43-49.

519 Lobanov, S.S., Hsu, H., Lin, J.F., Yoshino, T., Goncharov, A.F., 2017b. Optical signatures of low spin Fe³⁺ in
520 NAL at high pressure. *J. Geophys. Res.: Solid Earth* 122, 3565-3573.

521 Lobanov, S.S., Speziale, S., 2019. Radiometric Temperature Measurements in Nongray Ferropericlasite
522 With Pressure- Spin- and Temperature-Dependent Optical Properties. *J. Geophys. Res.: Solid Earth* 124,
523 12825-12836.

524 Manthilake, G.M., de Koker, N., Frost, D.J., McCammon, C.A., 2011. Lattice thermal conductivity of lower
525 mantle minerals and heat flux from Earth's core. *Proc. Natl. Acad. Sci. U.S.A.* 108, 17901-17904.

526 Mao, Z., Wang, F., Lin, J.F., Fu, S.Y., Yang, J., Wu, X., Okuchi, T., Tomioka, N., Prakapenka, V.B., Xiao, Y.M.,
527 Chow, P., 2017. Equation of state and hyperfine parameters of high-spin bridgmanite in the Earth's
528 lower mantle by synchrotron X-ray diffraction and Mossbauer spectroscopy. *Am. Mineral.* 102, 357-368.

529 McWilliams, R.S., Dalton, D.A., Mahmood, M.F., Goncharov, A.F., 2016. Optical Properties of Fluid
530 Hydrogen at the Transition to a Conducting State. *Phys. Rev. Lett.* 116, 255501.

531 Montoya, J.A., Goncharov, A.F., 2012. Finite element calculations of the time dependent thermal fluxes
532 in the laser-heated diamond anvil cell. *J. Appl. Phys.* 111, 112617.

533 Nimmo, F., 2015. 8.02 - Energetics of the Core A2 - Schubert, Gerald, in: Schubert, G. (Ed.), *Treatise on*
534 *Geophysics (Second Edition)*. Elsevier, Oxford, pp. 27-55.

535 Ohta, K., Onoda, S., Hirose, K., Sinmyo, R., Shimizu, K., Sata, N., Ohishi, Y., Yasuhara, A., 2008. The
536 electrical conductivity of post-perovskite in Earth's D'' layer. *Science* 320, 89-91.

537 Ohta, K., Yagi, T., Hirose, K., Ohishi, Y., 2017. Thermal conductivity of ferropericlasite in the Earth's lower
538 mantle. *Earth Planet. Sci. Lett.* 465, 29-37.

539 Ohta, K., Yagi, T., Taketoshi, N., Hirose, K., Kornabayashi, T., Baba, T., Ohishi, Y., Hernlund, J., 2012.
540 Lattice thermal conductivity of MgSiO₃ perovskite and post-perovskite at the core-mantle boundary.
541 *Earth Planet. Sci. Lett.* 349, 109-115.

542 Okuda, Y., Ohta, K., Hasegawa, A., Yagi, T., Hirose, K., Kawaguchi, S.I., Ohishi, Y., 2020. Thermal
543 conductivity of Fe-bearing post-perovskite in the Earth's lowermost mantle. *Earth Planet. Sci. Lett.* 547,
544 116466.

545 Okuda, Y., Ohta, K., Yagi, T., Sinmyo, R., Wakamatsu, T., Hirose, K., Ohishi, Y., 2017. The effect of iron
546 and aluminum incorporation on lattice thermal conductivity of bridgmanite at the Earth's lower mantle.
547 *Earth Planet. Sci. Lett.* 474, 25-31.

548 Panovska, S., Constable, C.G., Korte, M., 2018. Extending Global Continuous Geomagnetic Field
549 Reconstructions on Timescales Beyond Human Civilization. *Geochem. Geophys. Geosys.* 19, 4757-4772.

550 Runcorn, S.K., 1992. Polar Path in Geomagnetic Reversals. *Nature* 356, 654-656.

551 Shankland, T.J., Nitsan, U., Duba, A.G., 1979. Optical absorption and radiative heat transport in olivine at
552 high temperature. *J. Geophys. Res.* 84, 1603-1610.

553 Sinmyo, R., Pesce, G., Greenberg, E., McCammon, C., Dubrovinsky, L., 2014. Lower mantle electrical
554 conductivity based on measurements of Al, Fe-bearing perovskite under lower mantle conditions. *Earth*
555 *Planet. Sci. Lett.* 393, 165-172.

556 Stackhouse, S., Stixrude, L., Karki, B.B., 2015. First-principles calculations of the lattice thermal
557 conductivity of the lower mantle. *Earth Planet. Sci. Lett.* 427, 11-17.

558 Syassen, K., 2008. Ruby under pressure. *High Pressure Res.* 28, 75-126.

559 Tang, X.L., Ntam, M.C., Dong, J.J., Rainey, E.S.G., Kavner, A., 2014. The thermal conductivity of Earth's
560 lower mantle. *Geophys. Res. Lett.* 41, 2746-2752.

561 van der Hilst, R.D., de Hoop, M.V., Wang, P., Shim, S.H., Ma, P., Tenorio, L., 2007. Seismostratigraphy
562 and thermal structure of Earth's core-mantle boundary region. *Science* 315, 1813-1817.

563 Wicks, J.K., Jackson, J.M., Sturhahn, W., Zhang, D.Z., 2017. Sound velocity and density of
564 magnesiowustites: Implications for ultralow-velocity zone topography. *Geophys. Res. Lett.* 44, 2148-
565 2158.

566